Check for updates

Advanced Materials Technologies

ADVANCED MATERIALS TECHNOLOGIES
www.advmattechnol.com

RESEARCH ARTICLE OPEN ACCESS

Fully Printed Organic Electrochemical Transistors With Low-Resistance Electrodes on Planarized 3D-Printed Substrates

Mohamad Kannan Idris | Ali Eskandari | Saumik Dey Shovan | Gerd Grau

Department of Electrical Engineering and Computer Science, York University, Toronto, Canada

Correspondence: Gerd Grau (grau@yorku.ca)

Received: 29 July 2025 | **Revised:** 24 November 2025 | **Accepted:** 25 November 2025

Keywords: 3D Printing | dispense printing | fused deposition modeling (FDM) | inkjet printing | organic electrochemical transistors (OECTs) | PEDOT:PSS | printed electronics

ABSTRACT

This work presents a novel methodology for fabricating organic electrochemical transistors (OECTs) integrated with planarized 3D-printed substrates, offering a scalable approach to integrate functional electronics into 3D-printed systems. By combining fused deposition modeling (FDM) with in situ surface ironing, dispense printing for low-resistance silver electrodes, and inkjet printing for high-quality poly(3,4-ethylenedioxythiophene) polystyrene sulfonate (PEDOT:PSS) channels, we achieve high-performance transistors with an average transconductance (g_m) of 78.2 mS, one of the highest values reported in the literature. OECTs integrated with planarized 3D printed substrates are compared to devices fabricated on glass substrates and achieved comparable performance. The thick, low-resistance electrodes produced via dispense printing are critical for this performance, demonstrating the technique's suitability for OECT manufacturing. This study establishes a process for integrating OECTs with 3D-printed structures, paving the way for customizable, application-specific electronic devices. By addressing key challenges in material compatibility and integrated fabrication, this work contributes to advancing the fields of bioelectronics, wearables, and additive manufacturing.

1 | Introduction

Organic electrochemical transistors (OECTs) have emerged as a promising technology in the fields of biosensing, neuromorphic computing, and environmental monitoring, owing to their unparalleled sensitivity to ionic environments [1–5]. Unlike conventional field-effect transistors, OECTs rely on ionic gating through an electrolyte, which modulates the conductivity of a polymer-based channel material. This distinct mechanism allows for low-voltage operation and high amplification efficiency, measured by the transconductance (g_m), a critical performance metric for these devices. High g_m values enable OECTs to detect subtle ionic changes, making them highly effective for applications such as wearable health monitors, lab-on-a-chip systems, and neural interfaces [6]. Despite their promise, scalable manufacturing methods for OECTs that achieve high performance while integrating with 3D geometries remain an ongoing challenge. Integrating OECTs with 3D geometries expands their application scope by enabling seamless incorporation into customized, functional devices with intricate designs. This capability is particularly valuable for bioelectronics and lab-on-a-chip systems, where device geometry can play a critical role in fluidic interactions, ergonomic design, and spatial constraints.

The fabrication of OECTs traditionally relies on planar substrates such as glass or flexible polymers, employing techniques like

This is an open access article under the terms of the Creative Commons Attribution License, which permits use, distribution and reproduction in any medium, provided the original work is properly cited.

© 2025 The Author(s). Advanced Materials Technologies published by Wiley-VCH GmbH

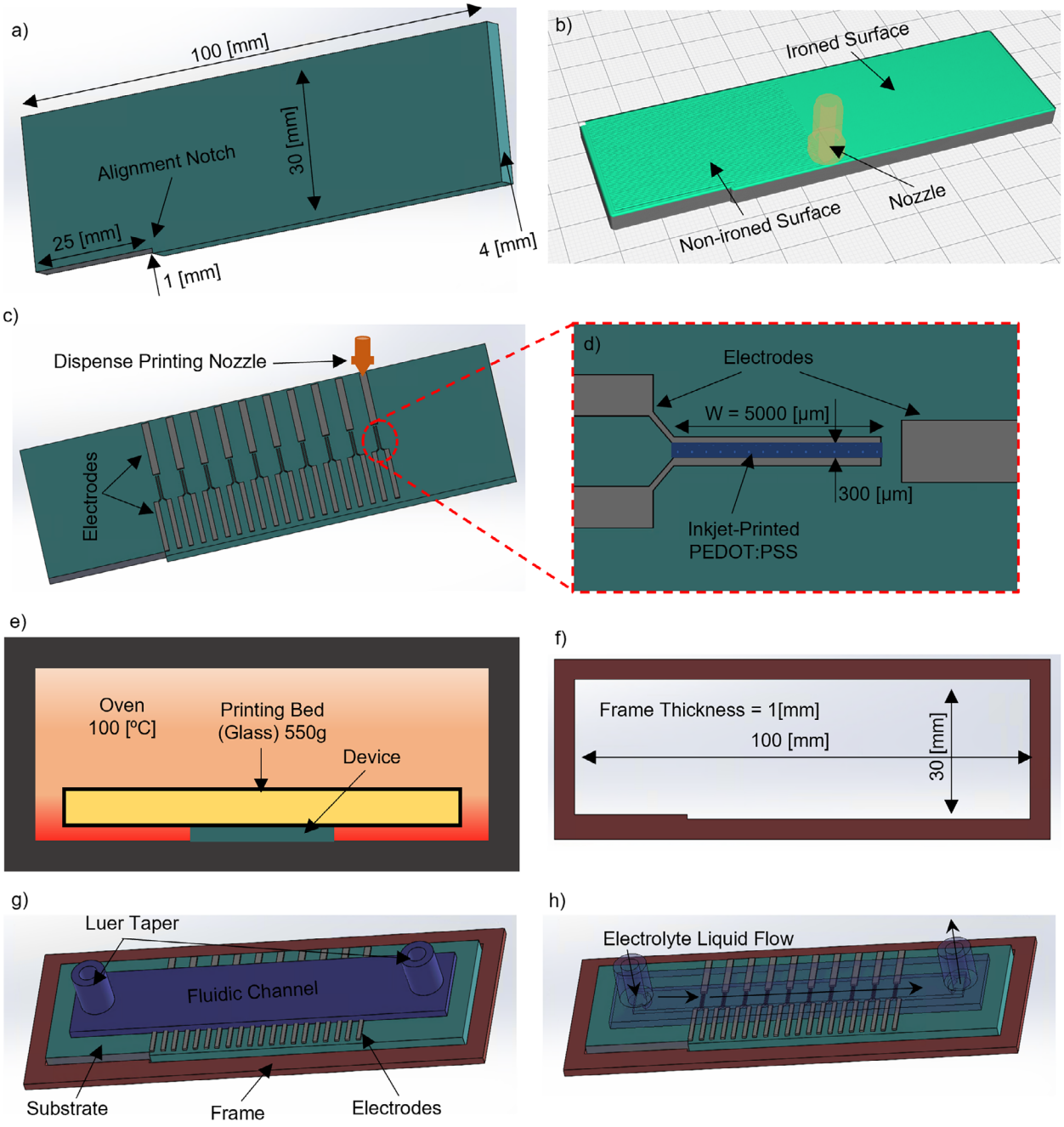


FIGURE 1 | Fabrication steps for the OECT integrated with a 3D-printed substrate. (a) The initial substrate design, including an alignment notch, printed using PLA on a Voxelab Aquila C2 FDM printer. (b) In situ surface ironing of the top layer to reduce roughness, enhancing compatibility with subsequent printing steps. (c) Dispense printing of silver electrodes using the NOVA printer, followed by curing at 100°C for 30 min. (d) Inkjet printing of the PEDOT:PSS semiconductor channel in a rectangular pattern using a custom drop-on-demand printer, with subsequent curing at 100°C for 20 min. (e) Correction of substrate warping by placing a 550 g glass weight during the final minutes of semiconductor curing. (f) Alignment frame printed to position the device for printing the microfluidic channel with a thickness of 1 mm. (g,h) The final printed OECT integrated with a microfluidic channel, featuring Luer taper inlet and outlet for syringe connection, designed for liquid electrolyte deposition and concentration studies.

photolithography, spin coating, or vapor deposition [7–9]. However, these methods are inherently limited by their reliance on multi-step processes, high cost, and incompatibility with 3D integration. Recent advances in additive manufacturing, particularly 3D printing, offer a transformative approach for integrating OECTs into different geometries. By combining electronics fabrication directly with 3D-printed structures, it is possible to overcome the constraints of traditional methods, paving the way for seamless integration of functional devices within customized, 3D objects.

Among the various additive manufacturing methods, fused deposition modeling (FDM) is widely recognized for its accessibility, cost-effectiveness, and versatility in creating 3Dobjects. FDM extrudes thermoplastic materials layer-by-layer to build 3D structures, making it a preferred choice for prototyping and

2365709x, 0, Downloaded from https://advanced.onlinelibrary.wiley.com/doi/10.1002/admt.202500627, Wiley Online Library on [08/12/2025]. See the Terms and Conditions (https://onlinelibrary.wiley.com/terms-and-conditions) on Wiley Online Library for rules of use; OA articles are governed by the applicable Creative Commons License

custom designs [10, 11]. However, the inherent layer-by-layer nature of FDM results in a rough surface texture with ridges and valleys, which poses significant challenges for integrating printed electronics. Conductive traces deposited on rough surfaces often suffer from discontinuities, varying thicknesses, and poor adhesion, which compromise the electrical and mechanical performance of the integrated device [12].

To mitigate these issues, surface smoothing techniques such as post-printing polishing, resin coatings, and laser ablation have been explored. However, these methods require additional processing steps, increasing fabrication time and cost [12–14]. A promising alternative for FDM is surface ironing, a technique in which the printer's hot nozzle remelts the topmost layer with fine line spacing, reducing surface roughness by as much as 96.6% as demonstrated in our earlier work. This process provides a cost-effective and streamlined solution, making FDM substrates compatible with electronics fabrication. Compared to resin coatings and mechanical polishing, ironing offers better integration with FDM workflows and eliminates the need for additional materials or tools [12].

For integrating OECTs, the deposition of conductive electrodes is a critical step, as their resistance directly impacts device performance, particularly the transconductance. Dispense printing, also known as direct-write printing, is an extrusion-based method that deposits high-viscosity inks, such as silver flake ink, onto various substrates. Unlike FDM, dispense printing creates fine conductive traces with low resistance. The technique involves extruding ink through a nozzle under controlled pressure to format patterns. This is particularly advantageous for OECT electrodes, where thickness and low sheet resistance are more important than lateral resolution [15–18].

Previous studies have highlighted the suitability of dispense printing for flexible and stretchable electronics, including antennas, resistors, and capacitors [16–24]. However, its application in OECT fabrication has been limited, often focusing on glass or flexible substrates. For example, dispense-printed electrodes on Teflon have demonstrated excellent durability but struggled with adhesion and uniformity on hydrophobic surfaces. The role of substrate preparation and printing parameters, such as nozzle height, pressure, and ink viscosity, has been extensively studied in our earlier work to optimize line quality [18]. Despite these advancements, integrating dispense printing with 3D printing for active devices remains an underexplored area.

Inkjet printing is another additive manufacturing technique with significant potential for OECT fabrication [1]. Unlike dispense printing, which excels in depositing thick, conductive traces, inkjet printing is ideal for forming thin, uniform films of organic semiconductors such as poly(3,4-ethylenedioxythiophene) polystyrene sulfonate (PEDOT:PSS). This polymer is widely used in OECTs due to its high conductivity, biocompatibility, and stability in aqueous environments [1, 2, 6, 9, 25–27]. Inkjet printing offers control over film thickness and geometry, enabling the fabrication of high-performance channels with consistent electrical properties [28–32].

Previous research has demonstrated the efficacy of inkjet-printed PEDOT:PSS for OECT channels on planar substrates. However, these studies primarily focus on glass substrates, with limited exploration of their integration with rougher surfaces [1, 9]. Combining inkjet and dispense printing provides a complementary approach, leveraging the strengths of each method to achieve high-performance OECTs. Dispense-printed silver electrodes can achieve low resistance, while inkjet-printed PEDOT:PSS ensures a uniform, high-quality semiconductor channel.

Efforts to combine 3D printing with electronics have primarily focused on embedding conductive traces or discrete components within 3D structures. While techniques like FDM with conductive filaments or SLA with resin fillers have enabled basic electrical functionality, these methods are constrained by low resolution and high resistivity [4, 33–35]. In contrast, our approach integrates high-performance OECTs into 3D-printed objects, addressing the limitations of previous methods. This is achieved through a multi-step process using all additive methods that combines FDM surface ironing, dispense printing of electrodes, inkjet printing of the semiconductor, and final 3D printing to create functional fluidic channels. Such a hybrid approach not only ensures compatibility between materials and processes but also opens new possibilities for integrating semiconductor devices with custom geometries. Whilst the OECT devices are printed in a planar fashion on one of the FDM printed layers, which is the most economical way of printing such devices, 3D objects can be built up around them by FDM. This approach does not require printing of the OECT devices onto curved or sloped surfaces, which could be a future extension of the process for full systems that may require 3D interconnects.

In this study, we present a novel methodology for integrating OECTs within 3D-printed objects, representing a significant advancement over previous works. Unlike earlier studies that focus on flat or flexible substrates, our approach integrates OECTs into potential 3D structures by leveraging the complementary strengths of FDM, dispense printing, and inkjet printing. The key contributions of this work include the integration of OECTs onto planarized 3D-printed surfaces to create fully additive, scalable OECTs with high performance, which is achieved through the right combination of device design, low-resistance electrode material, and print quality enabled by understanding of the printing process and optimized ironing of the FDM-printed surface. Additionally, the integration of functional OECTs within fluidic channels demonstrates seamless integration of electronics into 3D-printed objects. To provide a direct performance comparison and to investigate the influence of channel length on device behavior, OECTs were also fabricated on glass substrates. This approach establishes a process for integrating high-performance OECTs into 3D devices, with potential applications in bioelectronics, wearables, and medical devices. By addressing the challenges of surface roughness, material compatibility, and process scalability, this work paves the way for the next generation of integrated electronics.

2 | Materials and Methods

2.1 | Materials

The transistors were printed on borosilicate glass slides obtained from Ted Pella and 3D-printed substrates. The 3D-printed

2365709x, 0, Downloaded from https://advanced.onlinelibrary.wiley.com/doi/10.1002/admt.202500627, Wiley Online Library on [08/12/2025]. See the Terms and Conditions (https://onlinelibrary.wiley.com/terms-and-conditions) on Wiley Online Library for rules of use; OA articles are governed by the applicable Creative Commons License

substrates and fluidic channels for the OECTs were manufactured using polylactic acid (PLA) filament sourced from Polymaker. PLA was chosen for its biodegradability, ease of use in FDM 3D printing, and compatibility with the surface ironing process, which is crucial for achieving the smoothness required for electronics integration.

The electrodes were fabricated using a high-viscosity silver flake ink (Creative Materials 120-7 LPS), specifically designed for direct-write printing applications. This ink was selected for its ability to produce thick, low-resistance conductive traces upon curing, making it particularly suitable for OECTs where high transconductance is critical for performance.

For the semiconductor channel, the conductive polymer PEDOT:PSS was used. The base material used was a 1.3 wt.% PEDOT:PSS aqueous dispersion (Clevios PH 1000, Heraeus), which was further modified to enhance its printing properties and electrical performance. To improve the morphology and inkjet printing capabilities of PEDOT:PSS, 6 wt.% ethylene glycol (EG, Sigma–Aldrich) was added. This additive enhanced the electrical conductivity and mechanical flexibility of the printed films. Additionally, 0.1 wt.% dodecyl benzene sulfonic acid (DBSA, Sigma–Aldrich) was incorporated to stabilize the dispersion and optimize the fluid dynamics of the ink during printing. To ensure the long-term stability of the PEDOT:PSS films in aqueous environments, 1 wt.% (3-glycidyloxypropyl) trimethoxysilane (GOPS) was included as a cross-linking agent. GOPS rendered the polymer insoluble in water, significantly improving the durability of the semiconductor layer. This cross-linking also enhanced the hole and ion conductivity of the material, ensuring reliable operation of the OECTs under various conditions.

2.2 | Device Fabrication

The fabrication of the OECTs on 3D-printed substrates involved a multi-step process, as outlined in Figure 1. Each step was carefully optimized to ensure pattern formation, reliability, and compatibility across the different fabrication techniques employed.

The process began with the fabrication of the substrate using PLA and a Voxelab Aquila C2 FDM printer. The substrate was designed in SolidWorks 2023 and was sliced using Ultimaker Cura 5.4. The substrate design included an alignment notch for accurate positioning during subsequent steps. The design and dimensions of the substrate are shown in Figure 1a. To improve the surface quality, the top layer of the substrate was ironed in situ immediately after printing. This step significantly reduced surface roughness, as detailed in our earlier study on FDM surface ironing. The FDM printing and ironing settings, listed in Table 1, were optimized to achieve the smoothness necessary for reliable printing of conductive traces and are depicted in Figure 1b.

Following the ironing process, the electrodes were printed using dispense printing. The substrate was removed from the FDM printer bed and placed in a NOVA printer (Voltera, Waterloo, Canada) equipped with 100 µm diameter nozzles (Subrex, Carlsbad, United States). Key parameters, including nozzle height, dispense pressure, and printing speed, were adjusted to ensure high-quality line printing, as detailed in Table 2 and further explored in previous work [21]. The ink preheating temperature was set slightly above the heat generated by the dispensing tool's electronics to achieve a constant temperature. The dispense printing step is illustrated in Figure 1c. After printing, the electrodes were cured at 100°C for 30 min in an oven. While the substrate experienced minor warping in the Z direction during curing, this deformation did not affect the subsequent printing step, and it was corrected in the following steps.

Next, the semiconductor layer was fabricated. The PEDOT:PSS ink was deposited in a rectangular pattern onto the source, drain, and channel areas using a custom piezoelectric drop-on-demand (DOD) inkjet printer. The movement of the printer stage was controlled by a LabVIEW program (National Instruments, Austin, TX), ensuring precise alignment of the printhead. The printer utilized a nozzle (MJ-ATP-0160-8MX, Microfab Technologies, Inc., Plano, TX) with a 100 µm orifice. The drop spacing was maintained at 105 µm along each line, with a 50 µm gap between lines in the rectangular pattern, as shown in Figure 1d. Only one layer of semiconductor was printed in the channel. Following ink deposition, the ink pattern was cured at 100°C

TABLE 1 | FDM 3D printing parameters.

Printing parameter	Value
Nozzle size	0.4 (mm)
Layer height	0.2 (mm)
Top/bottom layer thickness	0.8 (mm)
Top layers	1
Bottom layers	1
All patterns	Zig Zag
Top/bottom line direction	0
Ironing line spacing	0.06 (mm)
Ironing flow	65 (%)
Ironing speed	75 (mm/s)
Infill density	100 (%)
Flow	100 (%)
Printing temperature	240 (°C)
Build plate temperature	60 (°C)

TABLE 2 | Dispense printing parameters.

Printing parameter	Value
Nozzle orifice diameter	100 (µm)
Nozzle height	50 (µm)
Dispense pressure	600 (a.u.)
Printing speed	500 (mm/min)
Relief pressure	80 (a.u.)
Dispense threshold	100 (%)
Relief threshold	0 (%)
Ink cartridge preheat temperature	35 (°C)

2365709x, 0, Downloaded from https://advanced.onlinelibrary.wiley.com/doi/10.1002/admt.202500627, Wiley Online Library on [08/12/2025]. See the Terms and Conditions (https://onlinelibrary.wiley.com/terms-and-conditions) on Wiley Online Library for rules of use; OA articles are governed by the applicable Creative Commons License

in an oven for 20 min. In the last five minutes of this curing step, a 550 g piece of 3D printing glass bed was placed on the substrate to correct any warping. This flattening step ensured the substrate met the flatness requirement of 0.1 mm for the final FDM printing step, as illustrated in Figure 1e. The final step involved printing the microfluidic channel. A frame was first printed on the FDM printer to serve as an alignment guide. The flattened device was positioned within the frame, and the fluidic channel was printed on top of the substrate with a height offset of 1.2 mm. The frame size and dimensions are shown in Figure 1f. The fluidic channel design included a Luer taper inlet and outlet for syringe connections. The completed device is shown in Figure 1g,h. Both the frame and the microfluidic channel were printed using the same FDM settings in Table 1 without ironing. To prepare the device for testing, 50 µl of a 100 mM solution of NaCl in water was deposited onto the source, drain, and gate electrodes using syringes. Sodium chloride was chosen as the electrolyte for its high ionic conductivity, stability, and compatibility with OECT operations. The ionic conductivity of NaCl ensures efficient gating and consistent device performance. Multiple NaCl concentrations, 100, 120, 140, 160, 180, and 200 mM, were used to study the effect of ionic concentration on device performance. Ten transistors were printed on the substrate to ensure statistical reliability in performance characterization. The transistor channel design featured a channel width of 5050 ± 15 µm and a channel length of 250 ± 21 µm, and semiconductor thickness of 1.86 µm ± 0.27 µm, as measured post-fabrication. These dimensions differed slightly from the original design specifications of 5000 µm for the width and 300 µm for the length due to ink spreading during the printing process. The behavior of ink flow and its effect on printed dimensions has been extensively studied in earlier research [18], highlighting the importance of optimizing printing parameters to achieve consistent and reproducible device geometries. These deviations were accounted for in the device characterization, ensuring accurate evaluation of transistor performance.

Control devices for comparison were fabricated on glass substrates. The glass substrates were sonicated in isopropanol, acetone, and deionized (DI) water, each for 10 min, and then dried with an air gun. The same process was used to print and cure the electrodes and semiconductor layer on the glass substrates as on 3D-printed PLA. No microfluidic channel was printed on the glass substrate. Five different transistor sizes were printed on glass by maintaining the channel width of 5050±15 µm and varying the channel length. The channel lengths used are 113 ± 7, 205 ± 16, 309 ± 10, 437 ± 12, and 526 ± 15 µm.

2.3 | Characterization

The dimensions of the transistors and electrodes were evaluated using an optical microscope (Keyence VHX-970F) to assess deviations from the intended design. The thickness of the printed organic semiconductor on glass was measured using a stylus profilometer (KLA-Tencor Alpha-Step D600) in the middle of the transistor along the width of the channel. This process was not possible on the 3D-printed substrates due to their surface roughness; thus the optical approach was used. Electrical measurements were conducted using a probe station equipped with a parameter analyzer (Keithley 4200A) to characterize the transistors' electrical performance. For each channel length, a total of ten transistors were printed and characterized to produce the average and standard deviation values and box plots of electrical figures of merit. The surface roughness of the PLA substrate after ironing was assessed using an optical profilometer (Bruker, United States). Surface roughness was measured at five different locations near the substrate's center, and the results were averaged. Detailed analysis of the profilometry data, including the methodology for calculating roughness and waviness, has been published previously [12]. This prior work also covers the MATLAB-based algorithm used for processing the scans. For this study, the roughness results were used to confirm the effectiveness of the ironing process in producing a smooth substrate suitable for subsequent printing steps. Contact angle measurements were taken using Kruss DSA10 contact angle measurement system. The images were processed using ImageJ software.

3 | Results and Discussion

The first step in evaluating the suitability of ironed PLA substrates for OECT fabrication is understanding their roughness. The measured average absolute roughness (Ra) of the surface is 847.3 ± 58 nm. The roughness of the surface consists of high and low-frequency roughness [12]. The high-frequency roughness represents the roughness of the surface that is generated from the line spacing of the ironed layer, printing deformities, and dust, since this device is not being manufactured in a cleanroom. The measured high-frequency roughness is 575.7 ± 18 nm. The low-frequency roughness represents the waviness of the surface, which is generated from the overall printing process. The measured low-frequency roughness is 485.1 ± 59 nm. These roughness values make the surface adequate for printing, and are a major improvement from the absolute roughness values of non-ironed PLA (10 ± 5 µm) [12]. Another step to evaluate the suitability of ironed PLA substrates for printing electronics is evaluating their wetting properties. This is achieved using contact angle measurements. Figure 2 summarizes the advancing and receding contact angle measurements for deionized (DI) water and PEDOT:PSS droplets on glass, ironed PLA, and non-ironed PLA substrates. Each data point is the average of 10 measurements, and the error bars represent the standard deviation of those measurements. These measurements provide insight into the influence of surface roughness and material composition on wettability, which is critical for ensuring uniform film deposition. Examples of the contact angle images are shown in Figures S1 and S2. As expected, the non-ironed PLA substrates exhibited higher advancing and receding contact angles and larger contact angle hysteresis compared to ironed PLA substrates, which, in turn, is higher than glass for both DI water and PEDOT:PSS. This behavior is attributed to the rough surface of non-ironed PLA compared to ironed PLA, as well as the rougher surface of ironed PLA compared to glass, which increases pinning effects and hysteresis. This highlights the significant reduction in surface roughness achieved through the ironing process [12]. The wetting behavior of PEDOT:PSS droplets on all three substrates closely mirrors that of DI water. This similarity arises from the water-based nature of the PEDOT:PSS dispersion, which governs its interaction with the substrate surfaces. These results demonstrate that ironed PLA substrates, despite their inherent roughness

2365709x, 0, Downloaded from https://advanced.onlinelibrary.wiley.com/doi/10.1002/admt.202500627, Wiley Online Library on [08/12/2025]. See the Terms and Conditions (https://onlinelibrary.wiley.com/terms-and-conditions) on Wiley Online Library for rules of use; OA articles are governed by the applicable Creative Commons License

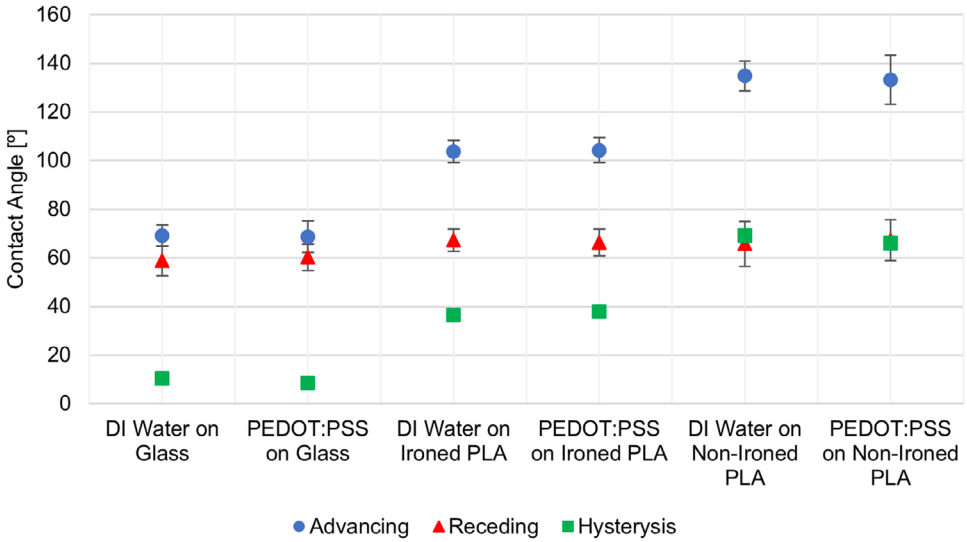


FIGURE 2 | Contact angle measurements of advancing and receding droplets of DI water and PEDOT:PSS on both glass and ironed PLA substrates. Each data point is the average of 10 measurements, and the error bars represent the standard deviation of those measurements.

compared to glass, provide adequate wetting for both DI water and PEDOT:PSS.

Figure 3 shows the fabrication design and resulting geometries of the organic electrochemical transistor (OECT) electrodes, showcasing the transition from the initial design to the final manufactured device. This analysis provides critical insights into the fidelity of the dispense and inkjet printing processes on ironed PLA substrates. Figure 3a illustrates the electrode design created using EAGLE software. The channel dimensions were specified as 5000 × 300 µm. However, as shown in Figure 3b, the printed electrodes exhibit deviations from these initial design parameters. Post-fabrication measurements of ten transistors revealed a channel width of 5050 ± 15 µm and a channel length of 250 ± 21 µm. These differences result from the behavior of the silver ink during deposition and curing, influenced by factors such as ink viscosity, dispense pressure, and surface properties. Small line edge roughness due to the remaining roughness of the ironed FDM printed surface can be observed. In order to avoid a bulge at the tip of the electrodes, which commonly forms in printed lines, and to ensure a uniform electrode width and channel length, a small fluid guiding feature was printed at the start of the lines. The printing behavior of the silver ink has been studied in-depth in previous research [18]. Figure 3c shows the inkjet printed PEDOT:PSS on glass for better visibility. The semiconductor film does not exhibit a strong coffee ring effect. The dispense printed electrodes on glass have an average thickness of 35 ± 1.7 µm and an average width of 250 ± 0.4 µm, making the thickness-to-width ratio 0.14 for all devices, as shown in Figure 3d. This electrode aspect ratio is significantly larger than inkjet-printed or evaporated electrodes [4, 9, 22], which results in a low sheet resistance of our dispense printed electrodes. For individual devices, the measured thickness of the semiconductor layer is highly uniform. The average thickness is 1.86 µm with a variation of ± 0.12 µm over the width of the device, as shown in Figure 3e. Between multiple devices, the thickness varies slightly, with a device-to-device variation of ± 0.27 µm. As shown in previous research [23], the silver sheet resistance is affected by the temperature used for curing. The printed silver electrodes undergo two curing phases, the first time after they are printed at 100°C for 30 min and the second time when the printed semiconductor is being cured at 120°C for 20 min. Sheet resistance was measured after each curing phase, and the results show that it decreased from 2.4 ± 0.4 mΩ/□ after the first phase to 2.2 ± 0.4 mΩ/□ after the second phase. Figure 3f provides a profilometric analysis of the device consisting of the printed electrodes and the PEDOT:PSS semiconductor layer deposited on top. The electrode lines exhibit a thickness of 36 ± 2 µm and a width of 251 ± 17 µm. The PEDOT:PSS layer, inkjet-printed across the channel and electrode regions, has a measured thickness of 2 ± 0.7 µm. Finally, Figure 3g shows the fully fabricated OECT device with PEDOT:PSS successfully integrated into the electrode architecture and the whole device integrated with a 3D printed microfluidic channel. The device represents the culmination of the multi-step fabrication process, with each step optimized to ensure smooth integration of functional layers. The combination of dispense printing for electrodes and inkjet printing for the semiconductor channel provides a scalable approach to OECT manufacturing on 3D substrates. These results confirm that the integration of dispense and inkjet printing on ironed PLA substrates produces devices with high geometric and functional fidelity. The observed variations emphasize the importance of optimizing printing parameters to ensure consistent and reproducible device fabrication.

Figure 4 presents the electrical characterization results (transfer and output characteristics) for a representative transistor, printed on a 3D-printed substrate, with a channel length of 250 µm. These measurements highlight the high transconductance achieved with the dispense printing method. Figure 4a shows the forward and backward sweep transfer characteristics of the OECT, plotting the drain current (I_D) as a function of the gate voltage (V_G) on a logarithmic scale at a constant drain voltage (V_D) of −1 V. Figure 4b shows the same transfer characteristics plotted on a linear scale. The g_m, calculated as the derivative of I_D with respect to V_G, reaches a peak value of 103 mS for this representative transistor. This high g_m value demonstrates the excellent electrical performance of the device, enabled by the thick and

2365709x, 0, Downloaded from https://advanced.onlinelibrary.wiley.com/doi/10.1002/admt.202500627, Wiley Online Library on [08/12/2025]. See the Terms and Conditions (https://onlinelibrary.wiley.com/terms-and-conditions) on Wiley Online Library for rules of use; OA articles are governed by the applicable Creative Commons License

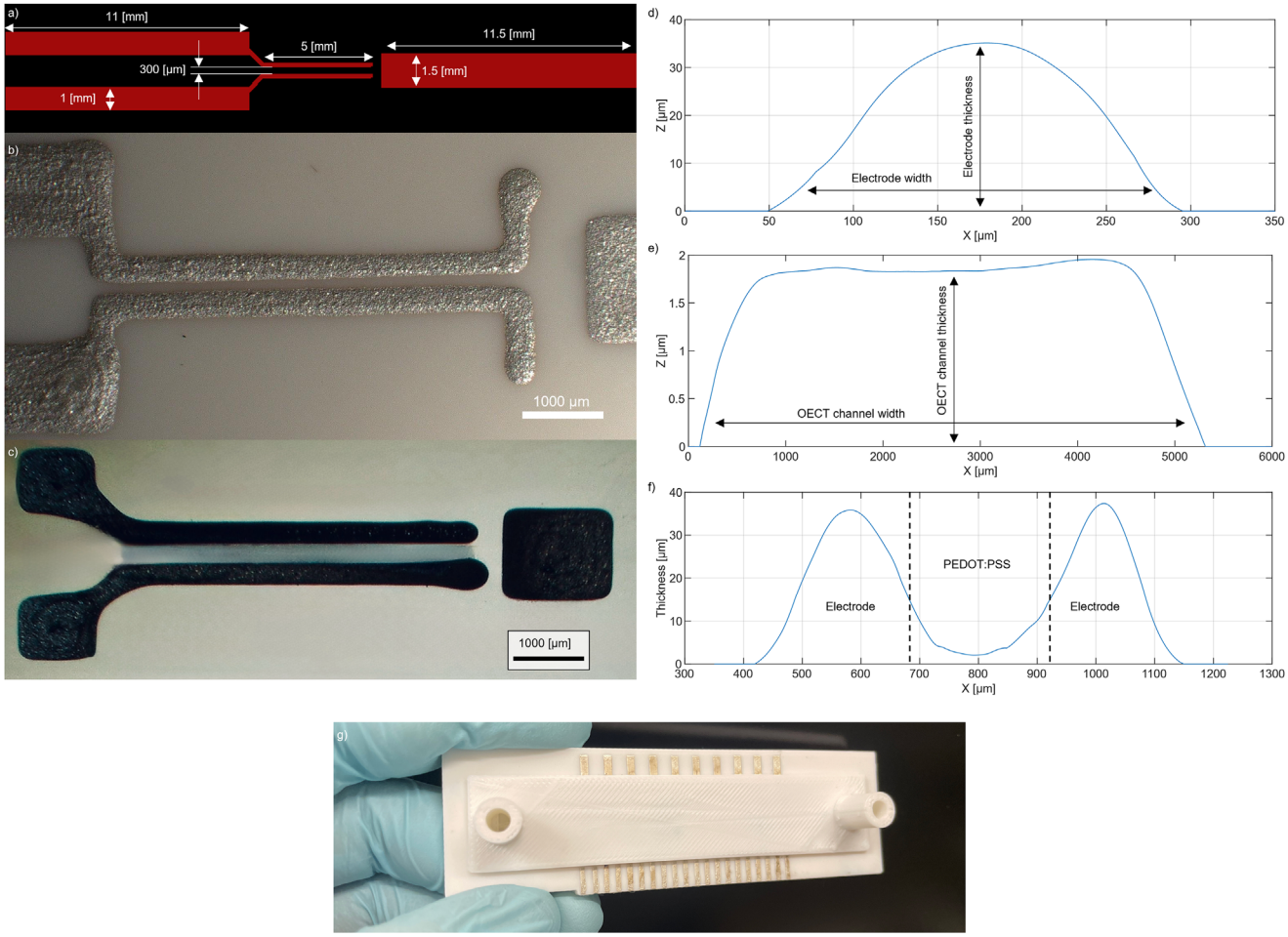


FIGURE 3 | Fabrication and dimensional analysis of printed electrodes for organic electrochemical transistors. (a) Electrode design created in EAGLE with a channel length of 300 µm and a channel width of 5000 µm. (b) Optical micrograph of the printed electrodes on ironed PLA substrates, highlighting dimensional deviations post-fabrication. The final channel dimensions measured were 250 ± 21 µm in length and 5050 ± 15 µm in width. (c) Optical micrograph of the control transistor printed on glass showing the inkjet-printed PEDOT:PSS channel. (d) Profile of the dispense printed electrodes on glass showing the thickness and width of the electrodes. (e) Profile of the inkjet-printed organic semiconductor on glass along the width of the OECT channel. (f) Profile of the device consisting of printed electrodes and PEDOT:PSS semiconductor layer, showing electrode thickness of 36 ± 2 µm, electrode width of 251 ± 17 µm, and PEDOT:PSS thickness of 2 ± 0.7 µm. (e) Image of the final OECT device with PEDOT:PSS and microfluidic channel printed onto the electrodes.

low-resistance silver electrodes deposited via dispense printing. The output characteristics, depicted in Figure 4c, illustrate the response of the drain current to varying drain voltages at different gate voltages. The linear and saturation regions observed in these curves confirm the expected behavior of OECTs, further validating the functionality of the fabricated devices. The current increase observed in the cut-off region is attributed to gate current leakage. To ensure statistical reliability, ten transistors were fabricated and characterized. The average peak g_m across all devices was 78.2 ± 19 mS. As a comparison with the OECTs on a 3D-printed surface, devices were also fabricated on glass with five different channel lengths. The transfer and output characteristics are shown in the Figure S3. The p-type OECT behavior of these devices on glass is very similar to devices on 3D-printed PLA. The devices with the smallest channel length (113 µm) exhibited an average transconductance of 98.2 ± 35.3 mS.

To understand the reason for such high transconductance values, the influence of the channel length on the performance of printed OECTs was systematically investigated, as depicted in Figure 5. The results, presented in the form of box plots, analyze three critical parameters: g_m, g_m normalized by channel dimensions (W/L), and the ON/OFF current ratio (I_{ON}/I_{OFF}) across the different channel lengths (113, 205, 309, 437, and 526 µm) on glass and 250 µm on 3D printed PLA. Figure 5a demonstrates the absolute transconductance values for OECTs with different channel lengths. The mean transconductance, indicated by red stars in the box plots, shows a trend where g_m generally decreases as the channel length increases. The devices printed onto 3D-printed PLA follow the same trend as on glass. The highest mean transconductance is observed at the shortest channel length (113 µm), as expected. The spread in the data suggests variability in the device fabrication or material consistency, which could influence the electrical properties. However, it is noteworthy that the variability of 3D-printed PLA is comparable to devices printed on glass. Contrary to the absolute transconductance, the normalized transconductance shown in Figure 5b exhibits an increasing trend with longer channel lengths. When transconductance is

2365709x, 0, Downloaded from https://advanced.onlinelibrary.wiley.com/doi/10.1002/admt.202500627, Wiley Online Library on [08/12/2025]. See the Terms and Conditions (https://onlinelibrary.wiley.com/terms-and-conditions) on Wiley Online Library for rules of use; OA articles are governed by the applicable Creative Commons License

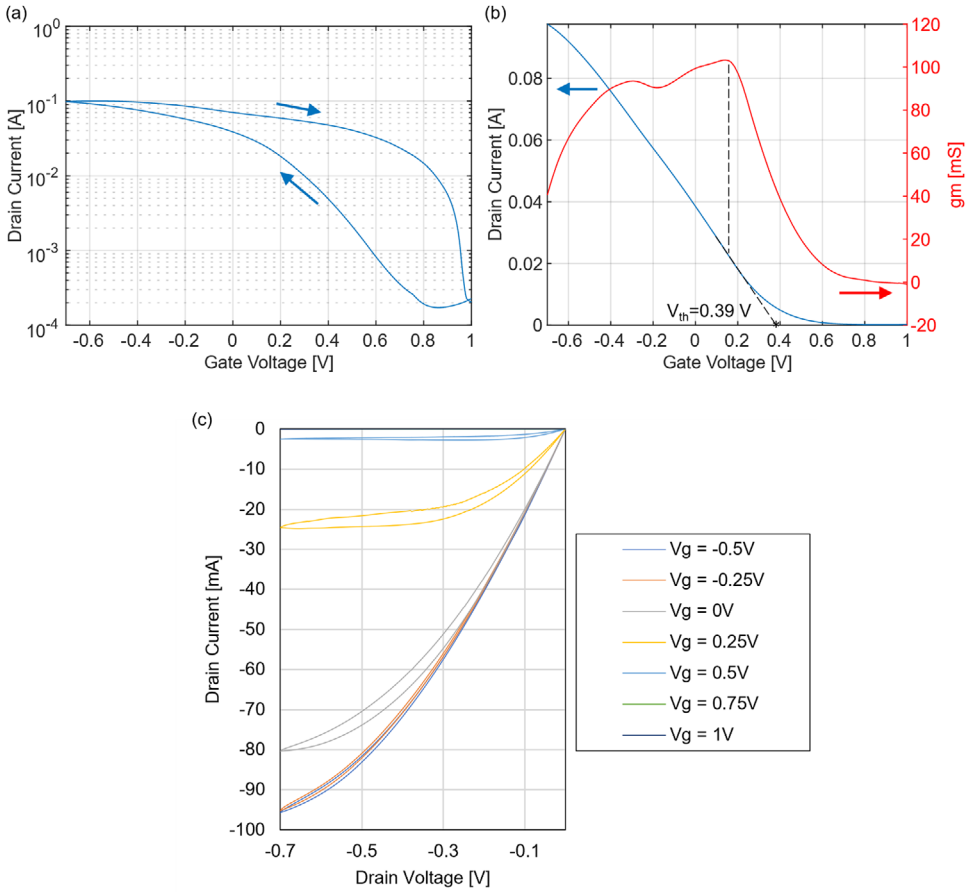


FIGURE 4 | Electrical characterization of printed organic electrochemical transistor on 3D-printed PLA with channel length 250 μm. (a) Transfer characteristics plotted on a logarithmic scale showing the forward and backward sweep drain current as a function of gate voltage. (b) Transfer characteristics plotted on a linear scale and the transconductance (g_m), highlighting a peak transconductance of 103 mS. The drain voltage (V_D) is −1 V. (c) Output characteristics with reverse and forward sweeps illustrating the drain current response to varying drain voltage at different gate voltages.

adjusted for the physical dimensions of the channel, longer channels exhibit improved performance relative to their size. Longer channel devices, while showing reduced absolute g_m, achieve higher g_m when normalized by channel geometry (W/L), indicating enhanced performance due to the reduced impact of contact resistance. Figure 5c shows the ON/OFF current ratio, a vital measure of the transistor's switching capabilities and power efficiency. Shorter channels exhibit a higher I_{ON} and, as a result, a higher I_{ON}/I_{OFF} ratio, which is advantageous for applications that demand fast switching and low power consumption. These findings illustrate that while shorter channels generally offer superior performance in terms of g_m and I_{ON}/I_{OFF} ratios, the increased normalized transconductance of longer channels suggests an impact of contact resistance.

The resistance characteristics of printed organic electrochemical transistors were analyzed using the transmission line method (TLM) to calculate contact resistance at different gate voltages from the variation of total device resistance with channel length [36]. In Figure 5d, the total resistance of the transistors is plotted against channel length for different gate voltages ($V_G = 0, -0.5$ V) at $V_D = -0.1$ V. Each data point is the average total resistance for 10 devices of the same channel length. A linear fit was performed on the total resistance vs. channel length for all tested gate voltages. By extrapolating these lines to a channel length of 0 μm, the intercepts provide values for the total contact resistance at each gate voltage, which are divided by two to estimate the contact resistance for one contact. The calculated contact resistances multiplied by the channel width are 2.1 ± 0.76 Ω.cm and 1.8 ± 0.05 Ω.cm for $V_G = 0$ and −0.5 V, respectively. These results indicate no significant difference in contact resistance between the examined gate voltages, and the differences are within the experimental error.

Figure 6 illustrates the electrical performance of one of the OECTs over 100 consecutive measurement cycles. The g_m and ON/OFF current ratio were measured during each run to evaluate the stability of the devices. In Figure 6a, the drain current is plotted vs. the gate voltage, showing the transfer characteristics change over 100 cycles. The results show a dip in performance after the first cycle, but the performance stabilizes afterwards. This behavior is evident in Figure 6b,c showing the average g_m and the ON/OFF current ratio consecutively over 100 cycles. The transistor produces a g_m of 197 mS in the first cycle, 133 mS in the 10th cycle, 125 mS in the 25th cycle, 119 mS in the 50th cycle, 116 mS in the 75th cycle, and finally 117 mS in the 100th cycle. The ON/OFF current ration dips from a value of 19 on the first cycle to an average of 11.8 in all the subsequent cycles. This result indicates stable transistor switching behavior over 100 cycles after an initial stabilization over the first cycles. Furthermore, this stability test

2365709x, 0, Downloaded from https://advanced.onlinelibrary.wiley.com/doi/10.1002/admt.202500627, Wiley Online Library on [08/12/2025]. See the Terms and Conditions (https://onlinelibrary.wiley.com/terms-and-conditions) on Wiley Online Library for rules of use; OA articles are governed by the applicable Creative Commons License

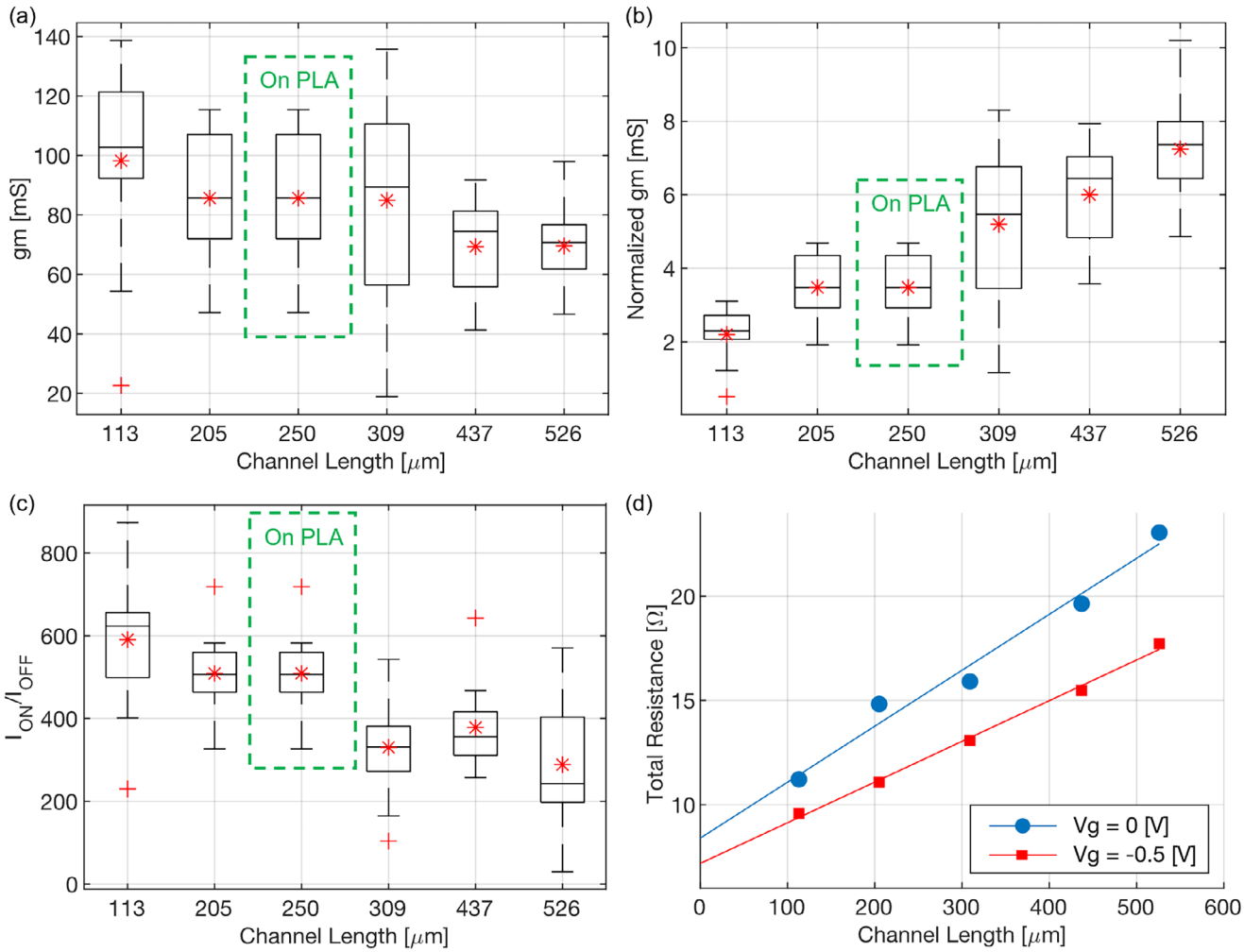


FIGURE 5 | Analysis of the influence of channel length on the performance of printed organic electrochemical transistors. (a) Absolute transconductance (g_m) values for OECTs with varying channel lengths, showing a decrease in g_m with increasing channel length. (b) Transconductance normalized by channel dimensions W/L, indicating an increasing trend with longer channel lengths. (c) ON/OFF current ratio (I_{ON}/I_{OFF}) across different channel lengths, with shorter channels exhibiting higher ratios. Red stars denote mean values, highlighting the trend and variability in device performance. (d) Resistance characterization using TLM. Total device resistance plotted against channel length for different gate voltages (V_G =0, −0.5 V), showing an increase in resistance with longer channel lengths. Linear fits indicate the trend for each gate voltage. Each data point is the average total resistance for 10 devices of the same channel length.

was conducted 440 days after the device was fabricated and stored under ambient conditions, indicating a long shelf life.

Figure 7a demonstrates the dynamic behavior of the organic electrochemical transistor (OECT) as the gate voltage (V_G) is switched from −1 V to 0.6 V. This transition highlights the role of ionic interactions in modulating the channel's conductivity when switching between the saturation and cut-off regimes. When V_G is set to −1 V, the device operates in the saturation regime, where ionic gating leads to high channel conductivity. Switching V_G to 0.6 V transitions the device to the cut-off regime, reducing channel conductivity as ions are expelled from the PEDOT:PSS layer. The sharp and consistent response during this transition underscores the efficiency and reliability of the ionic gating mechanism. There is typically a trade-off between the thickness of the organic semiconductor and the switching time of OECTs, as thicker films require more time for ions to penetrate and modulate conductivity. With this in mind, our measured switching time of 2 s for a 1.86 μm thick PEDOT:PSS film demonstrates efficient ionic transport. For comparison, Mangoma et al. reported a switching time of 10 s and g_m of 0.25 mS for a 2.15 μm thick film, and Nazeri et al. observed a 3 s switching time and g_m of 2.2 mS for a thickness of 1.8 μm [4, 9]. Figure 7b shows the stability of the drain current in both ON and OFF phases over an extended period of time of 1 h.

Figure S4 illustrates the relationship between the concentration of the NaCl electrolyte and the drain on-current of the OECT. The measurements were taken at six concentrations ranging from 100 to 200 mM, with five replicates for each concentration to ensure statistical reliability. The results show a clear positive correlation between the electrolyte concentration and I_{ON}. As the NaCl concentration increases, the ionic conductivity of the electrolyte improves, facilitating more effective ionic gating of the PEDOT:PSS channel. This enhanced gating increases the channel's conductivity, leading to higher on-current values. This

2365709x, 0, Downloaded from https://advanced.onlinelibrary.wiley.com/doi/10.1002/admt.202500627, Wiley Online Library on [08/12/2025]. See the Terms and Conditions (https://onlinelibrary.wiley.com/terms-and-conditions) on Wiley Online Library for rules of use; OA articles are governed by the applicable Creative Commons License

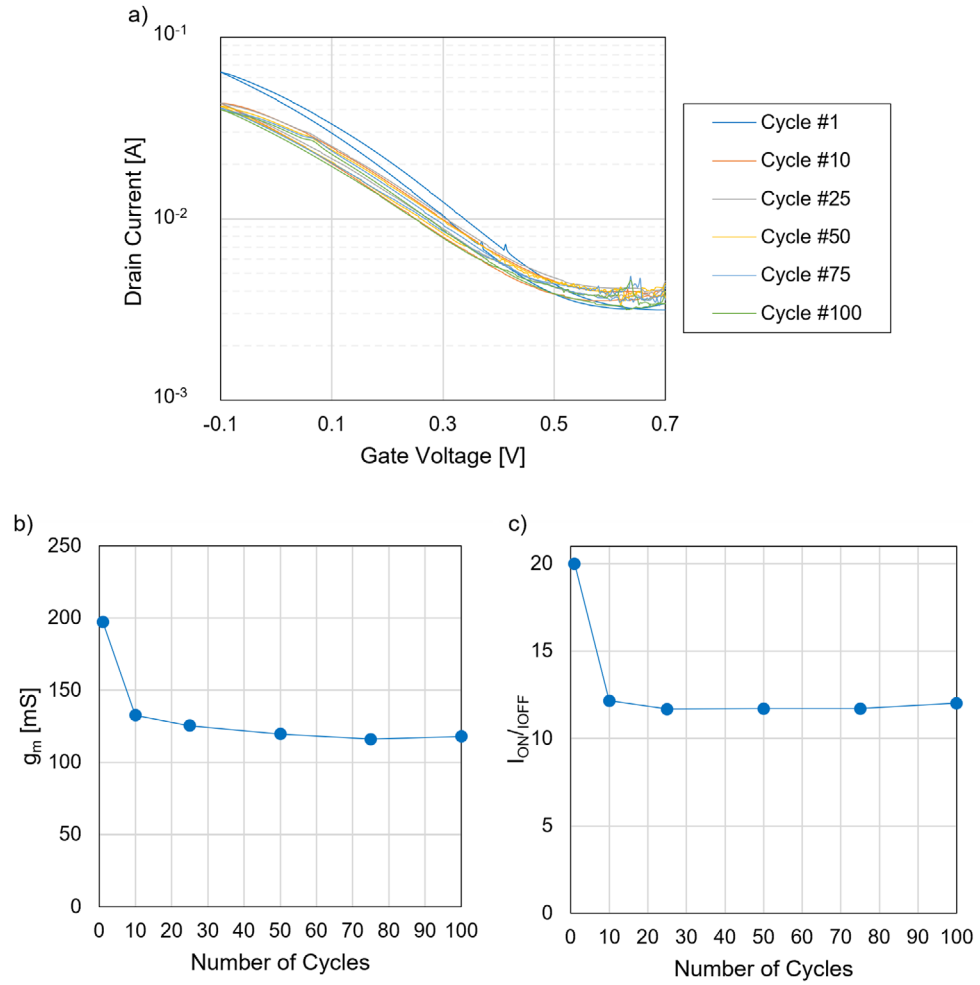


FIGURE 6 | The electrical characteristics of an organic electrochemical transistor for multiple measurements (cycles). (a) The change in the I_D-V_g current over 100 cycles. (b) The change of transconductance (g_m) over 100 cycles. (c) The change of ON/OFF current ratio (I_{ON}/I_{OFF}) over 100 cycles.

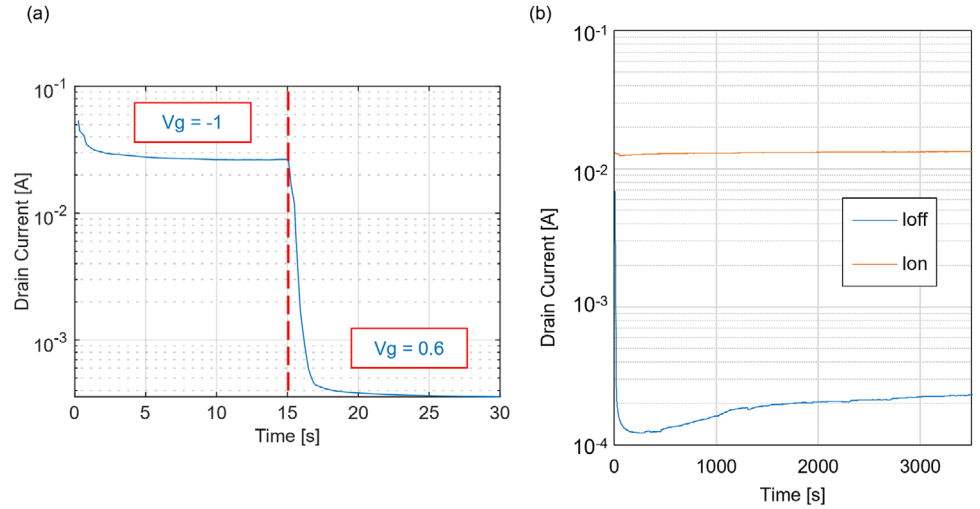


FIGURE 7 | (a) The drain current vs. time for $V_G = -1$ V and $V_G = 0.6$ V, representing the role of ions in the OECT when it transitions from the saturation to the cut-off regimes. (b) The drain ON and OFF current vs. time showing the stability of the device current for continuous operation over one hour.

2365709x, 0, Downloaded from https://advanced.onlinelibrary.wiley.com/doi/10.1002/admt.202500627, Wiley Online Library on [08/12/2025]. See the Terms and Conditions (https://onlinelibrary.wiley.com/terms-and-conditions) on Wiley Online Library for rules of use; OA articles are governed by the applicable Creative Commons License

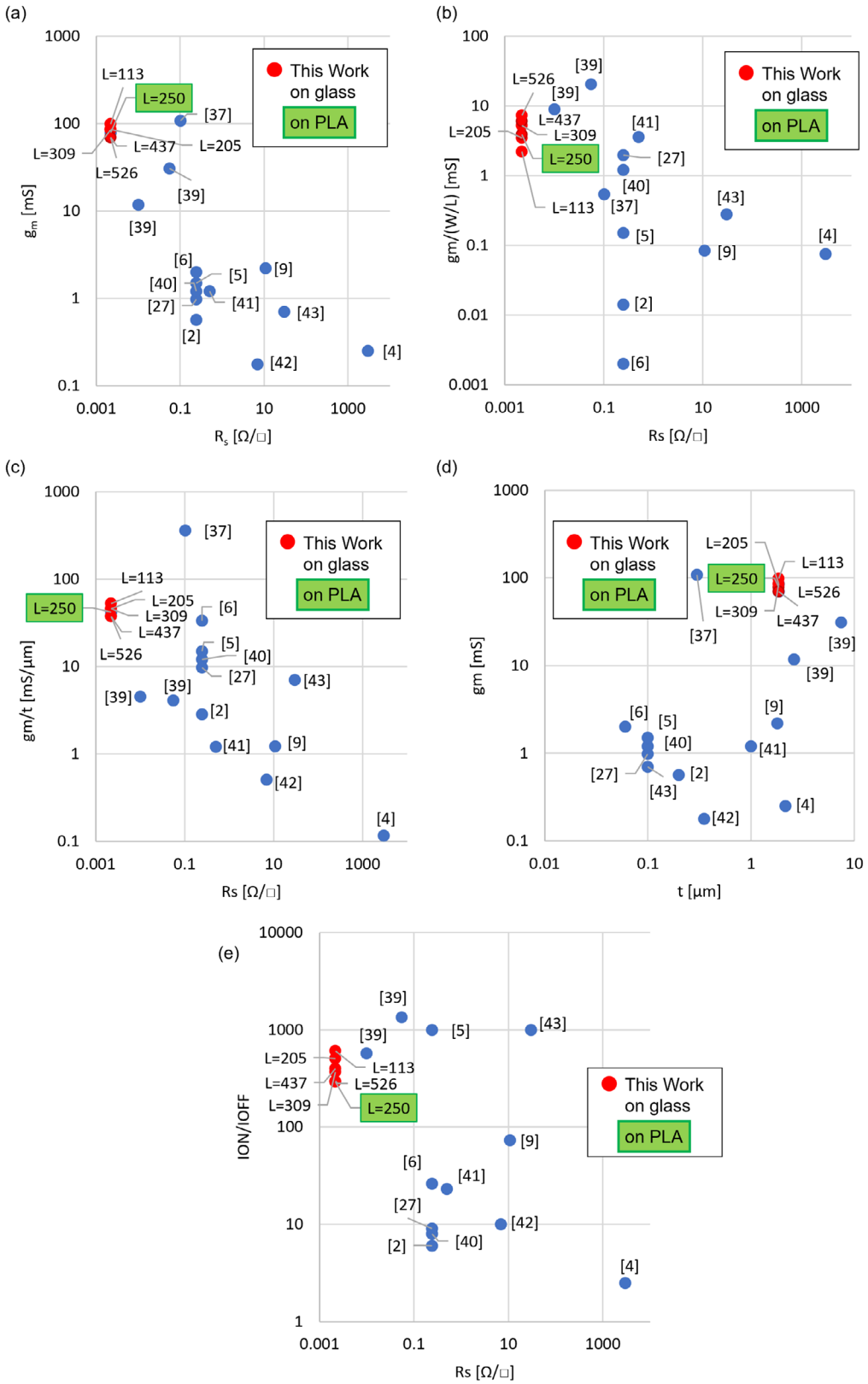


FIGURE 8 | Comparative analysis of transconductance (g_m) and I_{ON}/I_{OFF} of printed organic electrochemical transistors against other reported devices [2, 4, 5, 6, 9, 27, 37, 39, 40, 41, 42, 43]. (a) Transconductance (g_m) vs. sheet resistance (Rs) demonstrating superior g_m for our devices due to low sheet resistance. (b) Normalized transconductance (g_m) by width-to-length ratio (W/L), indicating our device's high performance relative to its dimensions. (c) Normalized transconductance (g_m) by channel thickness (t), showing optimal balance and high performance of our device. (d) Transconductance (g_m) as a function of channel thickness, where our device achieves the highest g_m compared to others with similar channel thicknesses, highlighting the effectiveness of our fabrication process. (e) On/off current ratio vs. sheet resistance, showing our device achieves a significantly high I_{ON}/I_{OFF} due to low sheet resistance.

2365709x, 0, Downloaded from https://advanced.onlinelibrary.wiley.com/doi/10.1002/admt.202500627, Wiley Online Library on [08/12/2025]. See the Terms and Conditions (https://onlinelibrary.wiley.com/terms-and-conditions) on Wiley Online Library for rules of use; OA articles are governed by the applicable Creative Commons License

trend demonstrates that OECT performance can be further optimized by changing the concentration of the electrolyte.

4 | Discussion

As shown in the electrical characterization results, our device exhibits a high g_m and current on/off ratio, which can be attributed to the low electrode sheet resistance. This is consistent with the findings of Marková et al., who systematically studied the effect of contact and serial resistance on the transconductance of OECTs using a similar TLM approach [37]. They showed that parasitic contact resistance significantly reduces the effective channel voltage and transconductance, especially in devices with short channels or highly conductive semiconductors. To mitigate this, they used planar devices with optimized gold contacts and achieved a low contact resistance of 6.5 Ω.cm and a high transconductance of 108 mS for a device geometry with channel width*thickness/length (*Wd/L*) of 60 µm. It is noteworthy that this g_m value is for a single champion device and not the average g_m over multiple devices because it was not reported. These numbers are comparable with our devices that have a contact resistance of 1.8 ± 0.05 Ω.cm and transconductance of 98.2 ± 35.3 mS averaged over ten devices, with the champion device exhibiting 133 mS for the smallest channel length on glass (*Wd/L* = 83 µm). The devices by Marková et al. consisted of interdigitated electrodes using silver-plated gold electrodes that were manufactured using physical vapor deposition. In contrast, our approach uses thick silver electrodes, which inherently lowers contact resistance due to their large cross-sectional area and low resistivity. This allows us to achieve low-resistance contacts without the need for complex geometries and complex fabrication processes, thereby validating and extending the theoretical framework established by Marková et al. using a fully printed, scalable method. Unfortunately, most other OECT literature sources do not report total and contact resistance for comparison. One exception uses laser-induced graphene (LIG) electrodes and reports an average g_m of 2.2 mS and contact resistance values between 40–150 Ω.cm and total resistance values between 150–700 Ω [9]. Another report deposited gold electrodes using sputtering that produced OECTs with contact resistance values between 10–80 kΩ.cm and an average g_m of 1.8 µS [38].

To still conduct a more comprehensive comparison with the literature, we analyzed literature sources in terms of the resistance of their electrodes (see Table 3). The devices are chosen according to the following criteria: all devices are OECTs, the semiconductor is PEDOT:PSS, and the values of g_m and I_{ON}/I_{OFF} are reported. Figure 8 shows a comparative analysis of g_m of our OECTs against the devices from the literature in Table 3.

Figure 8a shows that our devices achieve a significantly higher g_m compared to most other devices. The highest g_m of 108 mS is the device by Marková et al. discussed in the previous paragraph [37]. The devices demonstrated in our work achieve the highest g_m for fully printed devices. Other devices utilizing dispense-printed electrodes follow closely, but their g_m values are lower due to thinner electrodes (10 µm) and higher resistance [39]. Devices with LIG electrodes perform well but lag behind dispense-printed ones, partially due to their higher sheet resistance [9]. Devices employing inkjet-printed silver electrodes [25] or evaporated gold [27, 40] clusters in the midrange, reflecting the limitations of these methods in achieving low-resistance electrodes. At the lower end are devices fabricated using materials like carbon, PLA, or FTO due to their higher resistivity and sheet resistance. Generally, the graph indicates a trend where lower sheet resistance correlates with higher g_m values. The enhanced g_m can be attributed to multiple characteristics of the electrodes: low resistivity, large thickness, and the combined effect resulting in low sheet resistance. These factors contribute to the low ohmic resistance of the electrodes, which is essential for maintaining efficient charge transport in high-current, low-voltage OECTs. Dispense printing allows for the creation of high-thickness electrodes, enabling long electrode paths suitable for large channel width-to-length (W/L) ratios while preserving low resistance. This ensures that the ohmic resistance of the electrodes remains low, thereby enhancing the overall device performance. In Figure 8b, g_m is normalized by the width-to-length ratio (W/L) of the channel. Normalizing by W/L allows us to account for the geometric factors that influence the transconductance. Our device still demonstrates a superior normalized g_m compared to many other devices and is on par with the best devices in literature. This indicates that even when accounting for the device dimensions, our OECTs maintain high performance. For further comparison, the previously mentioned interdigitated device has a low normalized g_m due to its relatively high channel width [37]. Figure 8c presents g_m normalized by the channel thickness. In this plot, our device achieves one of the highest g_m normalized by channel thickness. Figure 8d displays g_m as a function of the channel thickness for different devices. Channel thickness is a critical parameter in OECTs as it directly affects the volume in which electronic charge transport occurs. Thicker channels have a larger capacitance, potentially increasing the transconductance, although there is a trade-off with switching speed. Our device benefits from a well-controlled channel thickness achieved through inkjet printing. This method allows for thicker and more uniform films compared to other methods, such as spin coating, which may struggle to produce uniform films at larger thicknesses. The data shows that our device achieves a large channel thickness and high g_m compared to others, indicating that our process successfully produces an active layer with a good thickness for high-g_m device operation. Figure 8e shows the current on/off ratio as a function of sheet resistance for various devices. Our device exhibits a high I_{ON}/I_{OFF} ratio, mainly due to the high I_{ON}, compared to other devices, indicating superior switching performance.

5 | Conclusions

This work presents a novel approach for integrating OECTs directly with planarized 3D-printed substrates, demonstrating a significant advancement in the fabrication of functional, embedded electronic devices. By leveraging FDM with in situ surface ironing, dispense printing for low-resistance silver electrodes, and inkjet printing for high-quality PEDOT:PSS channels, we successfully developed a scalable and fully additive process to create high-performance OECTs. The fabricated transistors exhibited excellent electrical performance, with an average transconductance of 78.2 mS on 3D-printed PLA, one of the highest values reported in the literature for similar devices. This achievement is attributed to the thick, low-sheet-resistance

2365709x, 0, Downloaded from https://advanced.onlinelibrary.wiley.com/doi/10.1002/admt.202500627, Wiley Online Library on [08/12/2025]. See the Terms and Conditions (https://onlinelibrary.wiley.com/terms-and-conditions) on Wiley Online Library for rules of use; OA articles are governed by the applicable Creative Commons License

TABLE 3 | OECTs in the literature using pristine PEDOT:PSS and the transistors that are presented in this work on 3D-printed PLA and glass.

Electrode material	Electrode fabrication method	Channel fabrication method	OSC thickness (μm)	Transistor channel width (μm)	Transistor channel length (μm)	Electrode thickness (μm)	Rs (Ω/□)	I_{ON} (mA)	I_{OFF} (mA)	I_{ON}/I_{OFF}	g_m (mS)	Voltages (V)	Refs.
Au	E-beam evaporator	Spin coating	0.1	5	10	0.1	0.244[a]	0.45	0.05	9	0.98	V_d = −0.6 V/V_g = 0.6 to 0 V	[27]
Au	Lift-off process	Spin coating	0.1	5	5	0.1	0.244[a]	4	0.5	8	1.2	V_d = −0.6 V/V_g = 5 to 0 V	[40]
Ag	Inkjet printing	Inkjet printing	1	1000	3000	0.2	0.5	0.46	0.02	23	1.2	V_d = −0.4 V/V_g = 1.6 to 0 V	[41]
Fluorine doped tin oxide (FTO)	Chemical etching	Spin coating	0.35	—	—	—	7	0.25	0.025	10	0.18	V_d = −0.6 V/V_g = 2.5 to 0 V	[42]
Carbon-filled polylactide (c-PLA)	3D printing	Inkjet printing	2.15	10000	3000	60	3000	0.125	0.05	2.5	0.25	V_d = −0.6 V/V_g = 0.6 to 0 V	[4]
LIG	Lasering process	Inkjet printing	1.8	5000	190	—	10.86	2.564	0.035	73.26	2.2	V_d= −1 V/V_g = 1 to −1 V	[9]
Au	Lift-off process	Spin coating	0.06	20000	20	0.1	0.244[a]	1.3	0.05	26	2	Vd = −0.5 V/Vg = −0.5 to 1 V	[6]
Au	Lift-off process	Spin coating	0.2	200	5	0.1	0.244[a]	0.6	0.1	6	0.57	Vd = −0.2 V/Vg = 0 to 0.8 V	[2]
Au	Evaporation	Spin coating	0.1	250	25	0.1	0.244[a]	1	0.001	1000	1.5	Vd = −0.1 V/Vg = 0.8 to −0.2 V	[5]

(Continues)

2365709x, 0, Downloaded from https://advanced.onlinelibrary.wiley.com/doi/10.1002/admt.202500627, Wiley Online Library on [08/12/2025]. See the Terms and Conditions (https://onlinelibrary.wiley.com/terms-and-conditions) on Wiley Online Library for rules of use; OA articles are governed by the applicable Creative Commons License

TABLE 3 | (Continued)

Electrode material	Electrode fabrication method	Channel fabrication method	OSC thickness (μm)	Transistor channel width (μm)	Transistor channel length (μm)	Electrode thickness (μm)	Rs (Ω/□)	I_{ON} (mA)	I_{OFF} (mA)	I_{ON}/I_{OFF}	g_m (mS)	Voltages (V)	Refs.
Carbon	Dispense printing	Felt-tip capillary printing	0.1	1000	400	—	30	—	—	1000	0.7	Vd = −0.2 V/Vg = 0.6 to −0.2V	[43]
Ag	Dispense printing	Dispense printing	2.6	912	694	10	0.01	4	0.007	570	11.7	Vd = −0.7 V/Vg = 0.6 to 0V	[39]
Ag	Dispense printing	Dispense printing	7.5	178	118	10	0.055	11	0.009	1130	30.7	Vd = −0.7 V/Vg = 0.6 to 0V	[39]
Ag plated Au	Physical vapor deposition	Spin coating	0.3	5000	25	0.2	0.102	—	—	—	108	Vd = −1 V/Vg = 0 to 1V	[37]
Ag	Dispense printing	Inkjet printing	1.86	5050	113	35	0.0022	84.6	0.14	604.29	98.2	V_d= −1 V/V_g= 1 to −0.7V	This work
Ag	Dispense printing	Inkjet printing	1.86	5050	205	35	0.0022	71.1	0.14	507.86	85.6	V_d= −1 V/V_g= 1 to −0.7V	This work
Ag	Dispense printing	Inkjet printing	2	5050	250	36	0.0022	29	0.1	290	78.2	V_d= −1 V/V_g= 1 to −0.5V	This work on PLA
Ag	Dispense printing	Inkjet printing	1.86	5050	309	35	0.0022	58.6	0.16	366.25	84.9	V_d= −1 V/V_g= 1 to −0.7V	This work
Ag	Dispense printing	Inkjet printing	1.86	5050	437	35	0.0022	63.4	0.16	396.25	69.3	V_d= −1 V/V_g= 1 to −0.7V	This work
Ag	Dispense printing	Inkjet printing	1.86	5050	526	35	0.0022	53.5	0.18	297.22	69.6	V_d= −1 V/V_g= 1 to −0.7V	This work

[a]These values are a lower bound estimate calculated based on the bulk resistivity of the material and the physical dimensions provided in the referenced manuscript

2365709x, 0, Downloaded from https://advanced.onlinelibrary.wiley.com/doi/10.1002/admt.202500627, Wiley Online Library on [08/12/2025]. See the Terms and Conditions (https://onlinelibrary.wiley.com/terms-and-conditions) on Wiley Online Library for rules of use; OA articles are governed by the applicable Creative Commons License

electrodes produced via dispense printing. Contact resistance was extracted from characterizing devices of varying channel lengths, and one of the lowest reported values was achieved. The devices also demonstrated stability over five measurement cycles. By combining different advanced additive manufacturing techniques with scalable materials and processes, this study establishes a process for integrating functional electronics with 3D-printed structures. This approach not only enhances the versatility of OECTs but also opens the door to a wide range of customizable, application-specific devices, paving the way for innovative developments in bioelectronics, wearable technology, and beyond.

Future work could explore the operation of these OECTs more extensively at lower drain-source voltages (below −1 V) to assess how key figures of merit, such as transconductance and on/off current ratio, evolve under lower-voltage operating conditions.

Acknowledgements

The authors acknowledge the support of the Natural Sciences and Engineering Research Council of Canada (NSERC), funding reference numbers RGPIN-2018-05857 and CREATE 565163-2022. The authors also thank the York University Microfabrication Facility (YMF) for providing access to essential fabrication and characterization equipment and facilities.

Conflicts of Interest

The authors declare no conflict of interest.

Data Availability Statement

The data that support the findings of this study are available from the corresponding author upon reasonable request.

References

1. W. AlChamaa and M. Khraiche, "High Performance Fully Inkjet-Printed Organic Electrochemical Transistor (OECT) Biosensor," *Journal of the Electrochemical Society* 169 (2022): 087518, https://doi.org/10.1149/1945-7111/ac88fa.

2. F. Hempel, J. K.-Y. Law, T. C. Nguyen, et al., "PEDOT:PSS Organic Electrochemical Transistor Arrays for Extracellular Electrophysiological Sensing of Cardiac Cells," *Biosensors & Bioelectronics* 93 (2017): 132–138, https://doi.org/10.1016/J.BIOS.2016.09.047.

3. S. Battistoni, C. Peruzzi, A. Verna, et al., "Synaptic Response in Organic Electrochemical Transistor Gated by a Graphene Electrode," *Flexible and Printed Electronics* 4 (2019): 044002, https://doi.org/10.1088/2058-8585/ab4dce.

4. T. N. Mangoma, S. Yamamoto, G. G. Malliaras, and R. Daly, "Hybrid 3D/Inkjet-Printed Organic Neuromorphic Transistors," *Advanced Materials Technologies* 7 (2022): 2000798, https://doi.org/10.1002/admt.202000798.

5. G. Frusconi, Z. M. Kovács-Vajna, and F. Torricelli, "Selective and Real-Time Ion Monitoring with Integrated Floating-Gate Organic Electrochemical Transistor Sensing Circuits," *Advanced Materials Technologies* 9 (2024): 2400301, https://doi.org/10.1002/admt.202400301.

6. K. Tang, W. Miao, and S. Guo, "Crosslinked PEDOT:PSS Organic Electrochemical Transistors on Interdigitated Electrodes with Improved Stability," *ACS Applied Polymer Materials* 3 (2021): 1436–1444, https://doi.org/10.1021/acsapm.0c01292.

7. V. Raghuwanshi, D. Bharti, I. Varun, A. K. Mahato, and S. P. Tiwari, "Performance Enhancement in Mechanically Stable Flexible Organic-Field Effect Transistors with TIPS-Pentacene:Polymer Blend," *Organic Electronics* 34 (2016): 284–288, https://doi.org/10.1016/j.orgel.2016.04.039.

8. N. Onojima, Y. Mori, T. Ozawa, T. Sugai, N. Akiyama, and S. Obata, "Flexible Organic Field-Effect Transistors Based on 6,13-Bis(Triisopropylsilylethynyl) Pentacene/Polystyrene Blend Film Prepared by Electrostatic Spray Deposition," *Japanese Journal of Applied Physics* 59 (2020): SDDA13, https://doi.org/10.7567/1347-4065/ab5c7a.

9. M. Nazeri, M. Ghalamboran, and G. Grau, "Laser-Induced Graphene Electrodes for Organic Electrochemical Transistors (OECTs)," *Advanced Materials Technologies* 8 (2023): 2300188, https://doi.org/10.1002/ADMT.202300188.

10. B. Wałpuski and M. Słoma, "Accelerated Testing and Reliability of FDM-Based Structural Electronics," *Applied sciences* 12 (2022): 1110, https://doi.org/10.3390/app12031110.

11. B. Akhoundi and A. H. Behravesh, "Effect of Filling Pattern on the Tensile and Flexural Mechanical Properties of FDM 3D Printed Products," *Experimental Mechanics* 59 (2019): 883–897, https://doi.org/10.1007/s11340-018-00467-y.

12. B. Neuhaus, M. K. Idris, P. Naderi, Y. El-Hajj, and G. Grau, "Low-Roughness 3D-Printed Surfaces by Ironing for the Integration with Printed Electronics," *Advanced Engineering Materials* 26 (2024): 2301711, https://doi.org/10.1002/adem.202301711.

13. M. Sardinha, C. M. S. Vicente, N. Frutuoso, M. Leite, R. Ribeiro, and L. Reis, "Effect of the Ironing Process on Abs Parts Produced by FDM," *Material Design & Processing Communications* 3 (2021), https://doi.org/10.1002/MDP2.151.

14. J. Butt, R. Bhaskar, and V. Mohaghegh, "Investigating the Effects of Ironing Parameters on the Dimensional Accuracy, Surface Roughness, and Hardness of FFF-Printed Thermoplastics," *Journal of Composites Science* 6 (2022): 121, https://doi.org/10.3390/jcs6050121.

15. M. K. Idris, P. Naderi, G. W. Melenka, and G. Grau, "Damage Location Sensing in Carbon Fiber Composites using Extrusion Printed Electronics," *Functional Composites and Structures* 3 (2021): 045001, https://doi.org/10.1088/2631-6331/ac3731.

16. M. K. Idris, J. Qiu, G. W. Melenka, and G. Grau, "Printing Electronics Directly onto Carbon Fiber Composites: Unmanned Aerial Vehicle (UAV) Wings with Integrated Heater for De-Icing," *Engineering Research Express* 2 (2020): 025022, https://doi.org/10.1088/2631-8695/ab8e24.

17. A. Cook, D. P. Parekh, C. Ladd, et al., "Shear-Driven Direct-Write Printing of Room-Temperature Gallium-Based Liquid Metal Alloys," Advanced Engineering Materials 21 no. 11 (2019): 1900400, https://doi.org/10.1002/ADEM.201900400.

18. M. K. Idris and G. Grau, "Dispense Printing of Silver Flake Inks on Hydrophilic and Hydrophobic Surfaces," *Advanced Engineering Materials* 26 (2024): 2401302, https://doi.org/10.1002/ADEM.202401302.

19. L. Friedrich and M. Begley, "Corner Accuracy in Direct Ink Writing with Support Material," *Bioprinting* 19 (2020): 00086, http://arxiv.org/abs/2003.05046.

20. K. B. Perez and C. B. Williams, "Combining Additive Manufacturing and Direct write for Integrated Electronics - A Review," in 24th International SFF Symposium - An Additive Manufacturing Conference, SFF (Springer, 2013), 962–979.

21. C. C. Ho, J. W. Evans, and P. K. Wright, "Direct Write Dispenser Printing of a Zinc Microbattery with an Ionic Liquid Gel Electrolyte," *Journal of Micromechanics and Microengineering* 20 (2010): 104009, https://doi.org/10.1088/0960-1317/20/10/104009.

22. Y. Yoon, S. Kim, D. Kim, S. K. Kauh, and J. Lee, "Four Degrees-of-Freedom Direct Writing of Liquid Metal Patterns on Uneven Surfaces," *Advanced Materials Technologies* 4 (2019): 1800379, https://doi.org/10.1002/admt.201800379.

2365709x, 0, Downloaded from https://advanced.onlinelibrary.wiley.com/doi/10.1002/admt.202500627, Wiley Online Library on [08/12/2025]. See the Terms and Conditions (https://onlinelibrary.wiley.com/terms-and-conditions) on Wiley Online Library for rules of use; OA articles are governed by the applicable Creative Commons License

23. M. S. Rahman and G. Grau, "Direct Writing of Stretchable Metal Flake Conductors: Improved Stretchability and Conductivity by Combining Differently Sintered Materials," *Flexible and Printed Electronics* 5 (2020): 025005, https://doi.org/10.1088/2058-8585/ab8f22.

24. M. K. Idris, B. Sarwar, Y. Rehman, and T. Imeci, "Rectangular Shaped Microstrip Patch Antenna with Multiple Slits and Slots," in 2017 25th Signal Processing and Communications Applications Conference (SIU), (IEEE, 2017) 1–4, https://doi.org/10.1109/SIU.2017.7960256.

25. F. Hempel, J. K.-Y. Law, T. C. Nguyen, et al., "PEDOT:PSS Organic Electrochemical Transistors for Electrical Cell-Substrate Impedance Sensing Down to Single Cells," *Biosensors & Bioelectronics* 180 (2021): 113101, https://doi.org/10.1016/J.BIOS.2021.113101.

26. L. M. M. Ferro, L. Merces, D. H. S. de Camargo, and C. C. B. Bufon, "Organic Electrochemical Transistors: Ultrahigh-Gain Organic Electrochemical Transistor Chemosensors Based on Self-Curled Nanomembranes," *Advanced Materials* 29 (2021): 2170223, https://doi.org/10.1002/adma.202170223.

27. S. Han, A. G. Polyravas, S. Wustoni, S. Inal, and G. G. Malliaras, "Integration of Organic Electrochemical Transistors with Implantable Probes," *Advanced Materials Technologies* 6 (2021): 2100763, https://doi.org/10.1002/admt.202100763.

28. D. Soltman and V. Subramanian, "Inkjet-Printed Line Morphologies and Temperature Control of the Coffee Ring Effect," *Langmuir* 24 (2008): 2224–2231, https://doi.org/10.1021/LA7026847.

29. F. Heinrich, T. Genco, and R. Lammering, "On The Mechanical Behavior of a Composite Stiffener with Inkjet-Printed Electronics," in 9th European Workshop on Structural Health Monitoring, EWSHM, Special Issue of e-Journal of Nondestructive Testing (eJNDT) ISSN 1435-4934, Vol. 23 no. 11, http://www.ndt.net/?id=23390.

30. T. Carey, S. Cacovich, G. Divitini, et al., "Fully Inkjet-Printed Two-Dimensional Material Field-Effect Heterojunctions for Wearable and Textile Electronics," *Nature Communications* 8 (2017): 1202, https://doi.org/10.1038/s41467-017-01210-2.

31. Z. Stempien, E. Rybicki, T. Rybicki, and J. Lesnikowski, "Inkjet-Printing Deposition of Silver Electro-Conductive Layers on Textile Substrates at Low Sintering Temperature by Using An Aqueous Silver Ions-Containing Ink for Textronic Applications," *Sensors and Actuators B: Chemical* 224 (2016): 714–725, https://doi.org/10.1016/j.snb.2015.10.074.

32. M. Mizukami, S.-I. Cho, K. Watanabe, et al., "Flexible Organic Light-Emitting Diode Displays Driven by Inkjet-Printed High-Mobility Organic Thin-Film Transistors," *Ieee Electron Device Letters* 39 (2018): 39–42, https://doi.org/10.1109/LED.2017.2776296.

33. H. Yang, W. R. Leow, and X. Chen, "3D Printing of Flexible Electronic Devices," *Small Methods* 2 (2018): 1700259, https://doi.org/10.1002/smtd.201700259.

34. D. Espalin, D. W. Muse, E. MacDonald, and R. B. Wicker, "3D Printing Multifunctionality: Structures with electronics," *The International Journal of Advanced Manufacturing Technology* 72 (2014): 963–978, https://doi.org/10.1007/s00170-014-5717-7.

35. Y. Khan, A. Thielens, S. Muin, J. Ting, C. Baumbauer, and A. C. Arias, "A New Frontier of Printed Electronics: Flexible Hybrid Electronics," *Advanced Materials* 32 (2019): 1905279, https://doi.org/10.1002/adma.201905279.

36. D. Natali, L. Fumagalli, and M. Sampietro, "Modeling of Organic Thin Film Transistors: Effect of Contact Resistances," *Journal of Applied Physics* 101 (2007): 014501, https://doi.org/10.1063/1.2402349/917455.

37. A. Marková, S. Stříteský, M. Weiter, and M. Vala, "Serial Resistance Effect on Organic Electrochemical Transistors″ Transconductance," *IEEE Sensors Journal* 23 (2023): 19417–19423, https://doi.org/10.1109/JSEN.2023.3296939.

38. A. F. Paterson, H. Faber, A. Savva, et al., "On the Role of Contact Resistance and Electrode Modification in Organic Electrochemical Transistors", *Advanced Materials* 31 (2019): 1902291, https://doi.org/10.1002/ADMA.201902291.

39. J. Fan, C. Montemagno, and M. Gupta, "3D Printed High Transconductance Organic Electrochemical Transistors on Flexible Substrates," *Organic Electronics* 73 (2019): 122–129, https://doi.org/10.1016/j.orgel.2019.06.012.

40. S. Y. Yeung, A. Veronica, Y. Li, and I. M. Hsing, "High-Performance Internal Ion-Gated Organic Electrochemical Transistors for High-Frequency Bioimpedance Analysis," *Advanced Materials Technologies* 8 (2023): 2201116, https://doi.org/10.1002/admt.202201116.

41. S. Demuru, C.-H. Huang, K. Parvez, et al., "All-Inkjet-Printed Graphene-Gated Organic Electrochemical Transistors on Polymeric Foil as Highly Sensitive Enzymatic Biosensors", *ACS Applied Nano Materials* 5 (2022): 1664–1673, https://doi.org/10.1021/ACSANM.1C04434.

42. J. M. Jeyavelan, F. Khurshid, M. Akhil, et al., "Highly Sensitive Organic Electrochemical Transistor for Detection of Stress-Induced Cation Leakage from Plant Cells," *Biosensors and Bioelectronics: X* 12 (2022): 100251, https://doi.org/10.1016/J.BIOSX.2022.100251.

43. R. Granelli, I. Alessandri, P. Gkoupidenis, et al., "High-Performance Bioelectronic Circuits Integrated on Biodegradable and Compostable Substrates with Fully Printed Mask-Less Organic Electrochemical Transistors," *Small* 18 (2022): 2108077, https://doi.org/10.1002/SMLL.202108077.

Supporting Information

Additional supporting information can be found online in the Supporting Information section.

Supporting File: admt70594-sup-0001-SuppMat.docx

2365709x, 0, Downloaded from https://advanced.onlinelibrary.wiley.com/doi/10.1002/admt.202500627, Wiley Online Library on [08/12/2025]. See the Terms and Conditions (https://onlinelibrary.wiley.com/terms-and-conditions) on Wiley Online Library for rules of use; OA articles are governed by the applicable Creative Commons License